

JGR Solid Earth

RESEARCH ARTICLE

10.1029/2021JB021648

Key Points:

- We present an alternating inversion scheme combining ambient noise traveltimes with teleseismic full-waveform inversion
- We demonstrate advantages of the alternating inversion over individual inversions using both synthetic and field data in central California
- Our model provides new constraints on the geometry of the Isabella Anomaly and helps decipher its origin

Supporting Information:

Supporting Information may be found in the online version of this article.

Correspondence to:

Y. Yang,
yingjie.yang@mq.edu.au







Citation:

Wang, K., Yang, Y., Jiang, C., Wang, Y., Tong, P., Liu, T., & Liu, Q. (2021). Adjoint tomography of ambient noise data and teleseismic P waves: Methodology and applications to central California. *Journal of Geophysical Research: Solid Earth*, 126, e2021JB021648. <https://doi.org/10.1029/2021JB021648>

Received 4 JAN 2021

Accepted 31 MAY 2021

Adjoint Tomography of Ambient Noise Data and Teleseismic P Waves: Methodology and Applications to Central California

Kai Wang^{1,2} , Yingjie Yang¹ , Chengxin Jiang³ , Yi Wang⁴ , Ping Tong^{5,6} , Tianshi Liu⁷, and Qinya Liu^{2,7} 

¹Department of Earth and Environmental Sciences, Macquarie University, Sydney, Australia, ²Department of Physics, University of Toronto, Toronto, Canada, ³Research School of Earth Sciences, The Australian National University, Canberra, Australia, ⁴State Key Laboratory of Geodesy and Earth's Dynamics, Innovation Academy for Precision Measurement Science and Technology, Chinese Academy of Sciences, Wuhan, China, ⁵School of Physical and Mathematical Sciences, Division of Mathematical Sciences, Nanyang Technological University, Singapore, Singapore, ⁶Asian School of the Environment, Nanyang Technological University, Singapore, Singapore, ⁷Department of Earth Sciences, University of Toronto, Toronto, Canada

Abstract Adjoint tomography has been recently applied to ambient seismic noise and teleseismic P waves separately to unveil fine-scale lithospheric structures beyond the resolving ability of traditional ray-based traveltimes tomography. In this study, we propose an inversion scheme that alternates between frequency-dependent traveltimes inversions of ambient noise surface waves and waveform inversions of teleseismic P waves to take advantage of their complementary sensitivities to the Earth's structure. We apply our method to ambient noise empirical Green's functions from 60 virtual sources, direct P and scattered waves from 11 teleseismic events recorded by a dense linear array (~7 km station spacing) and other regional stations (~40 km average station spacing) in central California. To evaluate the performance of the method, we compare tomographic results from ambient noise adjoint tomography, full-waveform inversion of teleseismic P waves, and the alternating inversion of the two data sets. Both applications to practical field data sets and synthetic checkerboard tests demonstrate the advantage of the alternating inversion over individual inversions as it combines the complementary sensitivities of the two independent data sets toward a more unified model. The three dimensional model from our alternating inversion not only shows major features of velocity anomalies and discontinuities in agreement with previous studies, but also reveals small-scale heterogeneities which provide new constraints on the geometry of the Isabella Anomaly and mantle dynamic processes in central California. The proposed alternating inversion scheme can be applied to other regions with similar array deployments for high-resolution lithospheric imaging.

Plain Language Summary Surface waves and teleseismic body waves map the Earth's internal structure from different angles and are complementary for constructing a unified model. Conventionally, these two data sets are combined based on the ray theory or other approximations of wave propagation theories, which might not image fine-scale heterogeneities of the medium. To overcome this limitation, we present a new inversion scheme by fitting surface waves from ambient noise and teleseismic compressional waves alternatively based on three-dimensional (3D) numerical simulations of the wave equation. The proposed method takes advantage of waveform information and accounts for more realistic 3D wave propagation effects, and thus it can resolve sub-wavelength structural heterogeneities. We demonstrate the advantage of the proposed alternating inversion over individual inversions using either synthetic or field data in central California. Our final model provides new constraints on the geometry of the subducted slab and helps decipher its origin. The proposed alternating inversion scheme can be applied to other regions for high-resolution lithospheric imaging.

1. Introduction

Traditional teleseismic traveltimes tomography using body waves has imaged a lot of high-resolution three-dimensional (3D) models of mantle structures (e.g., Aki et al., 1976; Hung et al., 2004; Montelli et al., 2004; Schmandt & Humphreys, 2010; Sigloch et al., 2008; van der Hilst et al., 1997). However, due

to the sub-vertical nature of ray paths of arriving teleseismic waves beneath receivers, traditional teleseismic traveltimes tomography has limited resolution at shallow depths (<50 km). On the other hand, surface wave tomography based on either earthquakes or ambient noise data can illuminate crustal and uppermost mantle structures at high resolution (e.g., Ekström et al., 1997; F.-C. Lin et al., 2007; Ritzwoller et al., 2002; Saygin & Kennett, 2010; Shapiro et al., 2005; Shen et al., 2013; Yang et al., 2007; Yao et al., 2006; Zheng et al., 2008); however, it has limited sensitivities to structures at greater depths (>~250 km). The apparent complementary sensitivities of surface waves and teleseismic body waves to the Earth's subsurface structures have motivated the development of inversion schemes that jointly invert the two data sets. Various applications based on surface wave dispersions and body wave traveltimes have been developed, and have demonstrated the feasibility of joint inversions for constructing a more unified model than separate inversions across different scales (e.g., Fang et al., 2016; Friederich, 2003; Guo et al., 2018; Jiang, Schmandt, Ward, et al., 2018; Nunn et al., 2014; Obrebski et al., 2011; West et al., 2004; Woodhouse & Dziewonski, 1984; Zhang et al., 2014). Nevertheless, such a traveltime-based joint inversion scheme has several limitations: (a) it is formulated based on ray theory or other approximation of wave propagation theories where structural sensitivity kernels are calculated without considering 3D lateral heterogeneities; (b) model parameters are usually velocity perturbations relative to a one-dimensional (1D) reference model rather than absolute values as teleseismic differential traveltimes are often used in the inversion; (c) traveltimes of primary phases (such as direct P and S waves) are most sensitive to long-wavelength structures (e.g., Liu & Gu, 2012), thus offering limited resolution.

Compared with traditional traveltime tomography, *adjoint tomography* based on 3D numerical modeling of the seismic wave propagation can account for more realistic 3D sensitivity kernels, and thus it can resolve sub-wavelength structural heterogeneities (Liu & Gu, 2012; Tromp, 2020; Virieux & Operto, 2009). Over the past decade, an increasing number of applications based on adjoint techniques have been conducted in various regions using earthquakes located within the model domain (e.g., Bozdağ et al., 2016; Chen et al., 2015; Fichtner et al., 2009; Krischer et al., 2018; Lloyd et al., 2020; Tao et al., 2018; C. Tape et al., 2009; Zhu et al., 2012), unveiling unprecedented details of the Earth's interior beyond the resolvability of traditional ray-based tomography. More recently, adjoint tomography has been further extended to applications using body waves from teleseismic events outside of the model domain (e.g., Beller, Monteiller, Operto, et al., 2018; Wang, Chevrot, et al., 2016) and empirical Green's functions from ambient seismic noise data (Chen et al., 2014; Gao & Shen, 2014; Lu et al., 2020; Wang et al., 2018, 2020; Yang & Gao, 2020; Zhang et al., 2018).

Teleseismic full-waveform inversion (TeleFWI) of high frequency P waves (including direct and scattered waves) has been demonstrated to be capable of resolving small-scale structures beneath dense linear arrays through the implementation of hybrid methods (C. Lin et al., 2019; Masson & Romanowicz, 2016; Monteiller et al., 2013, 2015; Pienkowska et al., 2020; Tong, Chen, et al., 2014; Tong, Komatitsch, et al., 2014). The hybrid methods couple a regional 3D numerical solver for a small target area with an external fast numerical/analytical method for a 1D background model. Utilizing the waveform information of scattered waves on both vertical and radial components, TeleFWI not only resolves small-scale local heterogeneities and sharp velocity discontinuities but also allows constraints on multiple model parameters, such as density, V_p and V_s . However, this method usually relies on the coherence of the scattered wavefields across stations which requires dense seismic arrays with small station spacing. For example, previous studies (Beller, Monteiller, Operto, et al., 2018; Wang, Chevrot, et al., 2016) have shown that TeleFWI based on 5–50 s P and coda waves recorded by a dense linear seismic array with ~8 km inter-station spacing, can resolve structural anomalies with a lateral dimension of ~20 km (close to the minimum wavelength). Although this technique can image high-resolution structures using data from dense seismic arrays, it suffers from increasing spatial aliasing effects when the station spacing becomes larger. In reality, dense seismic arrays with a station spacing of 10 km or less are usually deployed as linear arrays for receiver function analysis or migration studies only in selected regions around the globe. Most seismic arrays for tomographic studies are designed to be nearly evenly distributed over a region with a much coarser station spacing (≥ 30 km), such as the USArray Transportable Array and ChinArray. Nevertheless, Beller, Monteiller, Combe, et al. (2018) demonstrate that additional stations from other coarser seismic networks can help improve the lateral resolution and penetration depth of TeleFWI compared with only using a two-dimensional (2D) dense linear array.

Different from TeleFWI, the lateral resolution of ambient noise tomography mostly depends on station distribution as it relies on surface waves extracted from cross-correlations between station pairs. To date, there are mainly two approaches to perform ambient noise tomography based on 3D numerical simulations of the seismic wave equation. The first one assumes a cross-correlation function from ambient noise data can be approximated as the Green's function between a pair of stations, which is conventionally called as the empirical Green's function (Bensen et al., 2008; F.-C. Lin et al., 2007; Yao et al., 2006), hereafter EGF. Then, EGFs' traveltimes misfits with respect to synthetics from point-force virtual sources are inverted for 3D structures (Chen et al., 2014; Gao & Shen, 2014; Wang et al., 2019). This type of methods mainly takes advantage of realistic 3D structural sensitivity kernels to resolve local velocity heterogeneities, and measures time shifts in several narrow period bands. The other approach proposed by Sager et al. (2018) involves modeling the cross-correlation wavefield for a spatial distribution of noise sources (Ermert et al., 2017; Tromp et al., 2010) and performs both source and structural inversions, known as full-waveform ambient noise inversion (FWANI). FWANI requires noise sources to be located inside of the model domain, and thus it is currently only applied to a global-scale study (Sager et al., 2020). In this regional-scale study, we adopt the first approach to perform the ambient noise adjoint tomography (Chen et al., 2014; Wang et al., 2018), hereafter ANAT, which assumes that approximate Green's functions are retrieved from cross-correlations of ambient noise and does not involve noise source modeling. Since ANAT and TeleFWI have complementary constraints on resolving Vs structures, the two methods can be combined into the same framework of adjoint tomography. Zhang et al. (2020) investigated such a concept of joint inversion of ambient noise and teleseismic body waves based on 2D adjoint tomography. To our best knowledge, a joint inversion of ambient noise and teleseismic body waves in the framework of 3D adjoint tomography has not been implemented and applied to either synthetics or real data sets. Such joint inversions can take advantage of both an accurate 3D numerical solver and the iterative inversion scheme, and thus are expected to reduce the aforementioned limitations in traditional traveltimes tomography. In addition, TeleFWI also provides additional constraints on Vp and density structures which may help further improve the Vs image of ANAT.

Inspired by the success of joint surface-wave and teleseismic body-wave inversions in traditional traveltimes tomography (e.g., Guo et al., 2018; Nunn et al., 2014; Obrebski et al., 2011; Zhang et al., 2014), in this study we develop an alternating inversion scheme combining the complementary sensitivities of ANAT and TeleFWI. We apply the method to both synthetic and field data sets in central California (Figure 1a). We first demonstrate the advantages of the alternating inversion by comparing the resulting velocity models with those from separate inversions (ANAT and TeleFWI) in practical field data applications and 3D synthetic checkerboard tests. Then, the final model from the alternating inversion is compared with velocity models from traditional traveltimes tomography and also with structural interfaces mapped from receiver function analysis. In the end, we will discuss both the advantages and limitations of our alternating inversion in resolving small-scale lithospheric structures.

2. Methodology

2.1. Traveltimes and Waveform Inversions

For traveltimes adjoint tomography of ambient noise (i.e., ANAT), we seek to minimize the traveltimes misfits between EGFs from noise cross-correlations and synthetic Green's functions (SGFs) from point-force sources (Wang et al., 2019). In this study, we measure the frequency-dependent traveltimes misfits expressed as:

$$\phi^T = \frac{1}{2} \sum_{i=1}^N \int_{-\infty}^{+\infty} \frac{h_i(\omega)}{H_i} \left[\frac{\Delta T_i(\omega, \mathbf{m})}{\sigma_i} \right]^2 d\omega, \quad (1)$$

where \mathbf{m} denotes the model vector, $\Delta T_i(\omega, \mathbf{m})$ represents the frequency-dependent traveltimes difference between the i th pair of SGF and EGF with its uncertainty σ_i , $h_i(\omega)$ is a frequency-domain window normalized by $H_i = \int_{-\infty}^{+\infty} h_i(\omega) d\omega$, and N is the number of measurements. The detailed expression of adjoint source for multitaper traveltimes measurements are listed in Appendix C of C. H. Tape (2009).

Time-domain full-waveform inversion (FWI) seeks to minimize the least-squares waveform misfit function (ϕ) between N number of observed data and the corresponding synthetics expressed as:

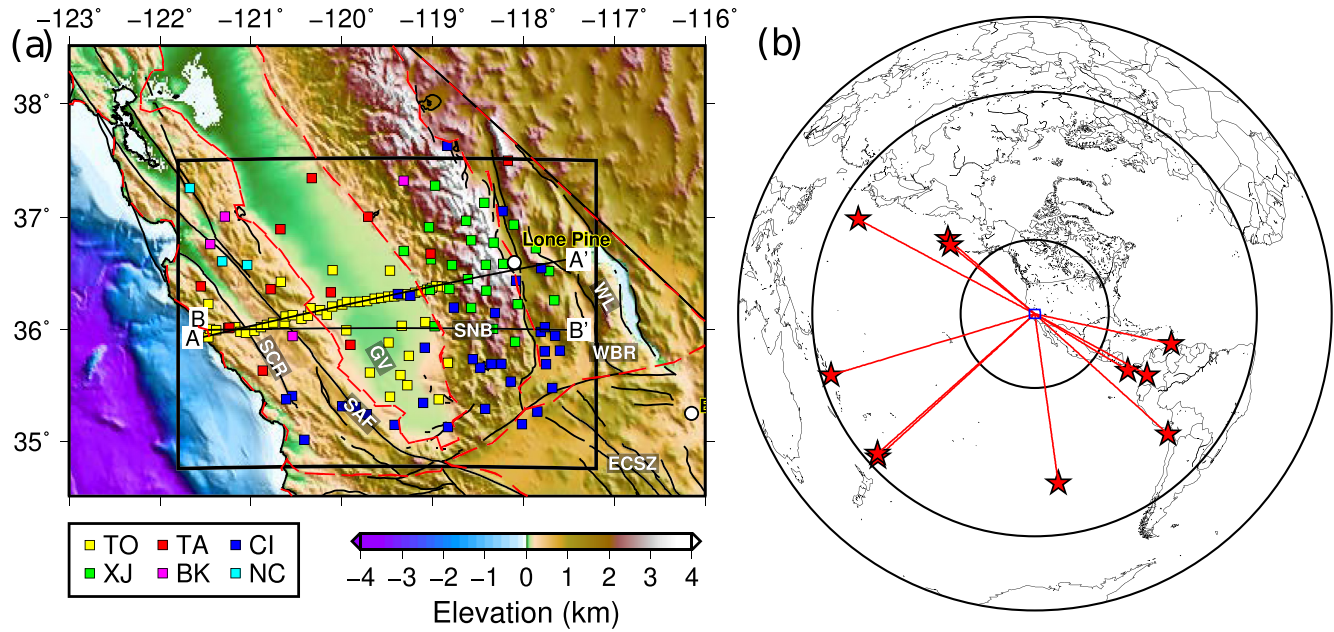


Figure 1. (a) Map of topography and station distribution in the study area. Stations from six seismic networks are plotted by rectangles filled with different colors as specified in the left bottom box. Black lines denote locations of the two cross-sections along which we will present our models in the following. The thick black box represents the simulation domain. Geologic abbreviations: SCR, Southern Coast Ranges; GV, Great Valley; SAF, San Andreas Fault; SNB, Sierra Nevada Batholith; WL, Walk Lane; WBR, Western Basin Ranges; ECSZ, Eastern California Shear Zone. (b) Location of the 11 teleseismic events (red stars) used in teleseismic full-waveform inversion. The two circles inside denote the boundaries of epicenter distances at 30° and 90°, and the blue rectangle is the study region.

$$\phi = \sum_{i=1}^N \int_{t1}^{t2} \frac{1}{2} \| \mathbf{u}_i(t) - \mathbf{d}_i(t) \|^2 dt, \quad (2)$$

where $\mathbf{d}_i(t)$ and $\mathbf{u}_i(t)$ denote the three-component waveforms of data and synthetic for the i th window between $(t1, t2)$. Due to the well-known source-structure tradeoff, accurate source wavelet estimation plays an important role in a successful FWI (Pratt, 1999; Virieux & Operto, 2009) and the effects of source-side surface-reflected multiples can be taken into account by convolving synthetics $\mathbf{u}_i(t)$ with an estimated source wavelet $W(t)$ (Bostock, 2004). Thus, a new waveform misfit function (ϕ^W) between data and the convolved synthetics is adopted in practice

$$\phi^W = \sum_{i=1}^N \int_{t1}^{t2} \frac{1}{2} \| \mathbf{u}_i(t) * W(t) - \mathbf{d}_i(t) \|^2 dt. \quad (3)$$

where the symbol $*$ represents the convolution operator. As demonstrated by Plessix (2006) and Beller, Monteiller, Operto, et al. (2018), the adjoint source of this new waveform misfit function is

$$f_i^{W\dagger}(t) = W(t) \star [\mathbf{u}_i(t) * W(t) - \mathbf{d}_i(t)], \quad (4)$$

where the symbol \star represents the correlation operator.

The adjoint sources are placed at receivers to generate the adjoint wavefield which interacts with the forward wavefield to generate sensitivity kernels defined in the linear relationship between the perturbations of misfit function ($\delta\phi$) and model variations

$$\delta\phi = \int [K_\rho(m)\delta \ln \rho + K_\alpha(m)\delta \ln \alpha + K_\beta(m)\delta \ln \beta] dV, \quad (5)$$

where $K_\rho(m)$, $K_\alpha(m)$, and $K_\beta(m)$ are the sensitivity kernels for density (ρ), Vp (α), and Vs (β) (Liu & Tromp, 2006; Tromp et al., 2005; Wang et al., 2019).

2.2. Alternating Inversion Algorithm

We adopt an alternating inversion algorithm originally developed for exploration seismic data by Sun et al. (2017), and reformulate it for deep Earth imaging based on the adjoint tomography of ambient noise and teleseismic data. The iterations of this method alternate between traveltimes and waveform inversions which has the advantage of avoiding nonphysical scaling factors between different data sets used in conventional joint inversions (e.g., Obrebski et al., 2011; Zhang et al., 2014). It is implemented through the following four steps:

1. At the beginning of the first iteration ($k = 0$), the initial model is set to be either a 1D reference model or a 3D model from previous seismic imaging studies.
2. Apply ANAT to minimize the traveltimes misfits (Equation 1) of Rayleigh waves between EGFs and SGFs, and obtain a new model \mathbf{m}_t .
3. Update the model as $\mathbf{m}_{k+1} = \mathbf{m}_t$. If the total misfit reduction over ANAT is less than a small value, such as 3% we choose in this study, iteration terminates; otherwise, set $k = k + 1$, and continue to the next step.
4. Apply TeleFWI to minimize the teleseismic P waveform differences (Equation 3) between observations and synthetics computed based on hybrid methods, and obtain a new model \mathbf{m}_{wf} .
5. Update the model by $\mathbf{m}_{k+1} = \mathbf{m}_{wf}$. If the total misfit reduction over TeleFWI is less than 3%, iteration terminates; otherwise, set $k = k + 1$, and go back to step 2.

3. Application to Seismic Data in Central California

We apply this alternating inversion method to image the lithospheric structure beneath central California to examine its feasibility and robustness. Our data sets consist of surface waves extracted from ambient noise cross-correlations and teleseismic P waveforms (including the direct P and its coda) recorded by 128 stations in central California (Figure 1a). These stations come from six seismic networks, including TO from the Central California Seismic Experiment (CCSE) deployed between 2013 and 2015, XJ from the Sierran Paradox Experiment in 1997, regional permanent networks (NC, CI, and BK) and the USArray Transportable Array (TA). In particular, the dense CCSE array (~7 km station interval) provides a high spatial sampling of teleseismic P scattered waves that are essential for resolving small-scale structures beneath the array. Other off-line stations sparsely distributed with an average of ~40 km inter-station distance help capture scattered waves in all directions more completely, and thus can improve the lateral resolution (Beller, Monteiller, Operto, et al., 2018).

3.1. Data Processing

We obtain ambient noise cross-correlation functions (CCFs) between station pairs from the TO and CI networks using the python package of NoisePy (Jiang & Denolle, 2020), in which the standard noise processing procedure of Bensen et al. (2007) is followed in the period band of 5–50 s. We also add CCFs of station pairs that are located within our study area and have been previously extracted by Xie et al. (2018) from other networks. In the data processing, we apply temporal normalization, spectral whitening, and long-term stacking (Bensen et al., 2007) to reduce effects of the inhomogeneous distribution of noise sources on the retrieval of EGFs. Furthermore, we fold and stack the positive and negative time lags of CCFs to obtain the symmetric components and only retain those CCFs with the signal-to-noise ratio (Bensen et al., 2007) larger than 10 for tomography. We convert symmetric CCFs to EGFs by taking a reversed time derivative of CCFs as done in Wang et al. (2018). In the end, 60 virtual sources are selected for the later inversion, resulting in 3167 ray paths that fairly uniformly cover our study region (Figure S1). In this study, we only use the Rayleigh waves from vertical-vertical component EGFs for adjoint tomography.

To obtain reliable scattered waves from teleseismic events, we apply a series of selection criteria for data quality control similar to those in Beller, Monteiller, Operto, et al. (2018), which are listed in the following:

Table 1
Event Information and Parameters of Plane Wave Injection, Including Event Origin Time, Longitude (Lon), Latitude (Lat), Depth, Back-Azimuth (Baz), and Incident Angle (Inc_ang) to the Center of the Array

Event ID	Origin time	Lon (°)	Lat (°)	Depth (km)	Baz (°)	Inc_ang (°)
5	April 1, 2014 23:46:47	-70.7691	-19.6097	25.0	131.460	18.09
12	June 23, 2014 19:19:15	-177.7247	-29.9772	20.	227.414	15.09
13	June 24, 2014 03:15:35	176.6981	52.2045	4.	310.964	24.08
27	October 9, 2014 02:14:31	-110.8112	-32.1082	16.54	171.613	19.02
29	December 8, 2014 08:54:52	-82.6865	7.9401	20.	120.220	24.69
37	May 30, 2015 11:23:02	140.4931	27.8386	664.	297.892	15.32
42	August 15, 2015 07:47:06	163.8226	-10.8968	8.	253.108	15.03
45	July 9, 1997 19:24:13	-63.4860	10.5980	19.9	102.334	21.73
46	September 2, 1997 12:13:22	-75.7499	3.8490	198.7	118.403	22.65
51	September 20, 1997 16:11:32	-177.6240	-28.6830	30.0	228.525	15.16
58	June 17, 1997 21:03:04	-179.3320	51.3470	33.0	309.119	24.60

1. Event Magnitudes ≥ 5.8 .
2. Epicentral distances to the center of the study region within 30° – 90° .
3. Hypocentral depths in the range of 0–30 km or 180–1000 km.
4. Individual traces with high signal-to-noise ratio (SNR).
5. Spatial coherent signals on both vertical and radial components across the array.
6. Waveforms with cross-correlation coefficients greater than 0.90, with respect to the array stack trace.

In the above steps, the first three criteria are used to select appropriate teleseismic events and the latter three are for picking high-quality waveforms on the receiver side. The last event selection criterion on hypocentral depth is to ensure that teleseismic waveforms are less contaminated from source-side surface reflections, such as the pP phase. According to the event selection criteria, we first download 345 teleseismic events from the global earthquake catalog using the program SOD (Owens et al., 2004). For each event, we collect three-component waveforms within time windows defined as 2 min before and 3 min after the direct P arrivals predicted by the AK135 model (Kennett et al., 1995). We then remove the instrument response, mean values, linear trends from the five-min time series, and rotate north and east components to radial and transverse components. Afterward, the pre-processed vertical and radial component waveforms of each event are visually inspected by the open-source software AIMBAT (Lou et al., 2013), and only those meet the data selection criteria (4–6) are retained. Note an iterative cross-correlation and stack algorithm is adopted in the AIMBAT package to calculate of the SNR, array stack trace, and cross-correlation coefficient for each seismogram. In total, we select 11 teleseismic events (Figure 1b) that satisfy the above data selection criteria for the following inversion. The detailed information of these 11 events is listed in Table 1.

3.2. Inversion Procedures

We perform all the forward and adjoint simulations based on the open-source spectral-element method (SEM) package, SPECSEM3D (Komatitsch & Vilotte, 1998; Peter et al., 2011) and the adjoint-state technique (Liu & Tromp, 2006). The simulation domain (Figure 1a) extends from 121.8°W to 117.2°W (~ 400 km), from 34.75°N to 37.5°N (~ 320 km), and from the surface to 220 km in depth. Its mesh has 80 and 60 elements in longitudinal and latitudinal directions respectively, and 25 layers in depth. The mesh is irregular with an element size of 5 km at the top (0–30 km) and 10 km at the bottom (30–220 km), giving a minimum resolving period of 3.5 s and a maximum time step of 0.03 s. In our inversion, we choose a time step of 0.025 s, a 120 s duration to simulate teleseismic P waves and a 170 s duration for surface waves.

Following the algorithm outlined in Section 2.2, the alternating inversion starts from a smoothed AK135 model (Kennett et al., 1995) (Figure S2) and proceeds by alternating ANAT and TeleFWI inversions to update the density and velocity structures. For ANAT, we follow similar inversion procedures as described in

Wang et al. (2018). We first place vertical point-force sources with a Gaussian source time function of 1.0 s half duration at the surface to generate vertical-component SGFs at receivers. Then, EGFs and SGFs are filtered at three narrow period bands: namely 6–15 s, 10–20 s, and 15–35 s. A multi-taper technique (e.g., C. Tape et al., 2009; Zhou et al., 2004) is adopted to measure the frequency-dependent traveltimes difference (Equation 1) between each EGF-SGF pair within the surface-wave time window determined by its phase velocity dispersion. The corresponding adjoint sources are calculated accordingly.

For forward simulations in TeleFWI, we adopt a hybrid method, FK-SEM, to compute the response in the simulation domain to the teleseismic wavefield from a plane wave injection. The FK-SEM method interfaces the numerically efficient frequency-wavenumber (FK) calculations for a 1D background model outside the domain with the accurate spectral-element computations for 3D models within the domain (Tong, Chen, et al., 2014; Tong, Komatitsch, et al., 2014). The initial wavefronts of the injected plane waves start from a reference point beneath the center of the array where incident angles and back-azimuths are also calculated for the various events as listed in Table 1. The depth of the reference point is defined at 400 km so as to ensure the initial wavefronts of the 11 teleseismic events do not enter the boundaries of the local simulation domain. The predicted arrival times of direct P waves from a plane wave are given by the travel-time delays between the initial wavefront reference point and receivers computed for the AK135 model (see Appendix A for details). In order to compare data with the synthetics, waveforms of observed teleseismic P waves are first aligned by subtracting the reference direct P arrivals predicted from the AK135 model, and then shifted by the predicted first arrivals from the initial wavefronts to receivers. We then apply a time domain deconvolution method (e.g., Kikuchi & Kanamori, 1982; Lay et al., 2009) in conjunction with principal component analysis (PCA) (e.g., Halldor & Venegas, 1997) to obtain the source wavelet signature from vertical components (Beller, Monteiller, Operto, et al., 2018; Wang, Chevrot, et al., 2016). Finally, we measure waveform differences between the data and synthetics convolved with the source signature as illustrated in Equation 3. Figure 2 shows an example of the general processing procedures similar to those used by Wang, Chevrot, et al. (2016), as summarized in the following four steps:

1. Data and synthetic waveforms are first filtered between 5 and 50 s. Observed data are also normalized by the maximum of the record section (Figure 2a) to balance the displacement amplitudes from earthquakes of different magnitudes in the inversion.
2. Based on the time-domain iterative deconvolution method (e.g., Kikuchi & Kanamori, 1982; Lay et al., 2009), the synthetics on the vertical component are deconvolved from their corresponding data to obtain the candidate source wavelets (Figure 2b).
3. PCA is applied to these candidate source wavelets to obtain different data modes (i.e., principal components) and the first mode which accounts for at least 80% contribution is regarded as the average source wavelet signature (Figure 2c).
4. The synthetics on both vertical and radial components are convolved with this average source wavelet and then compare with corresponding shifted observed data to calculate waveform differences and adjoint sources (Figure 2d).

For each teleseismic event or virtual source, we calculate the event kernel by injecting the adjoint sources at receivers based on the adjoint-state method (Liu & Tromp, 2006). Then, all event kernels are summed, preconditioned and smoothed to obtain the final misfit gradient for model updating. A preconditioner given by the square root of depth (Wang, Chevrot, et al., 2016) is used to approximate the Hessian matrix to accelerate the convergence of the inversion. In the first several iterations, the horizontal and vertical radii of the 3D Gaussian function used to smooth the gradient are 20 and 10 km, respectively. Then, they are reduced to smaller values of 10 and 5 km to resolve smaller scale structures in later iterations. During the inversion, the optimization is achieved through the L-BFGS algorithm (Chap. 9, Nocedal & Wright, 2006) and a line search method is used to determine the optimal step length for model updating.

To demonstrate the advantage of our alternating inversion framework, we also conduct two additional separate inversions either only using ambient noise data or only using teleseismic data. The separate inversions also begin with the smoothed AK135 model and use the same inversion parameters as the alternating inversion including the smoothing radii and step lengths. In total, we conduct three inversions: (a) traveltimes adjoint tomography of ambient noise surface waves (i.e., ANAT); (b) waveform inversion of teleseismic P and scattered waves (i.e., TeleFWI); (c) alternating inversion using two data sets (i.e., Alter).

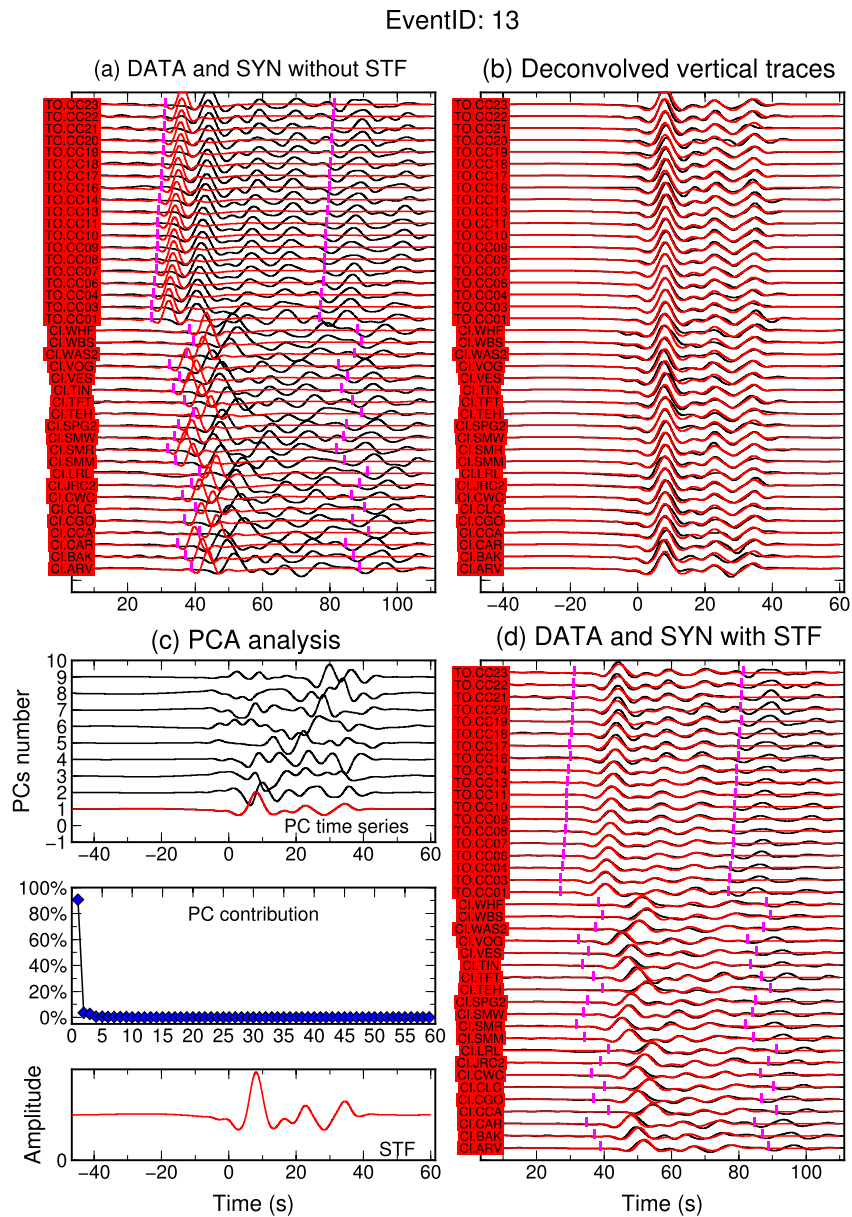


Figure 2. An example of the four processing steps to obtain the average source wavelet signature (i.e., STF, source time function) and waveform differences for event 13. (a) Data (black) and synthetics (red) filtered at the period band of 5–50 s. (b) Candidate STFs (black) obtained by deconvolving the synthetic from the data based on the time domain deconvolution method. The waveforms in red color denote the primary principal component (PC) of the STFs in c. (c) Top: Time series of the first nine PCs; Middle: Contribution of each PC; Bottom: the primary PC used as the average STF. (d) Data (black) and new synthetics (red) convolved with the average STF. Purple bars in (a) and (d) represent the time windows $[-5, 45]$ s relative to direct P arrivals) for measuring the waveform differences.

3.3. Synthetic Tests and Model Resolution

We first conduct several numerical experiments to demonstrate the advantage of the alternating inversion over separate inversions and to assess the model resolution. Synthetic data is computed for checkerboard models with $\pm 12\%$ perturbations relative to the smoothed AK135 background model, and simulated with the same source time functions as those used in the practical inversions. Then, we conduct the alternating inversion and two separate inversions following the same inversion procedures described in Section 3.2. Figure 3 displays the recovered checkerboard models with anomaly sizes of 40 km from ANAT, TeleFWI, and the alternating inversion, respectively. It is clear that surface waves from this study are mostly sensitive

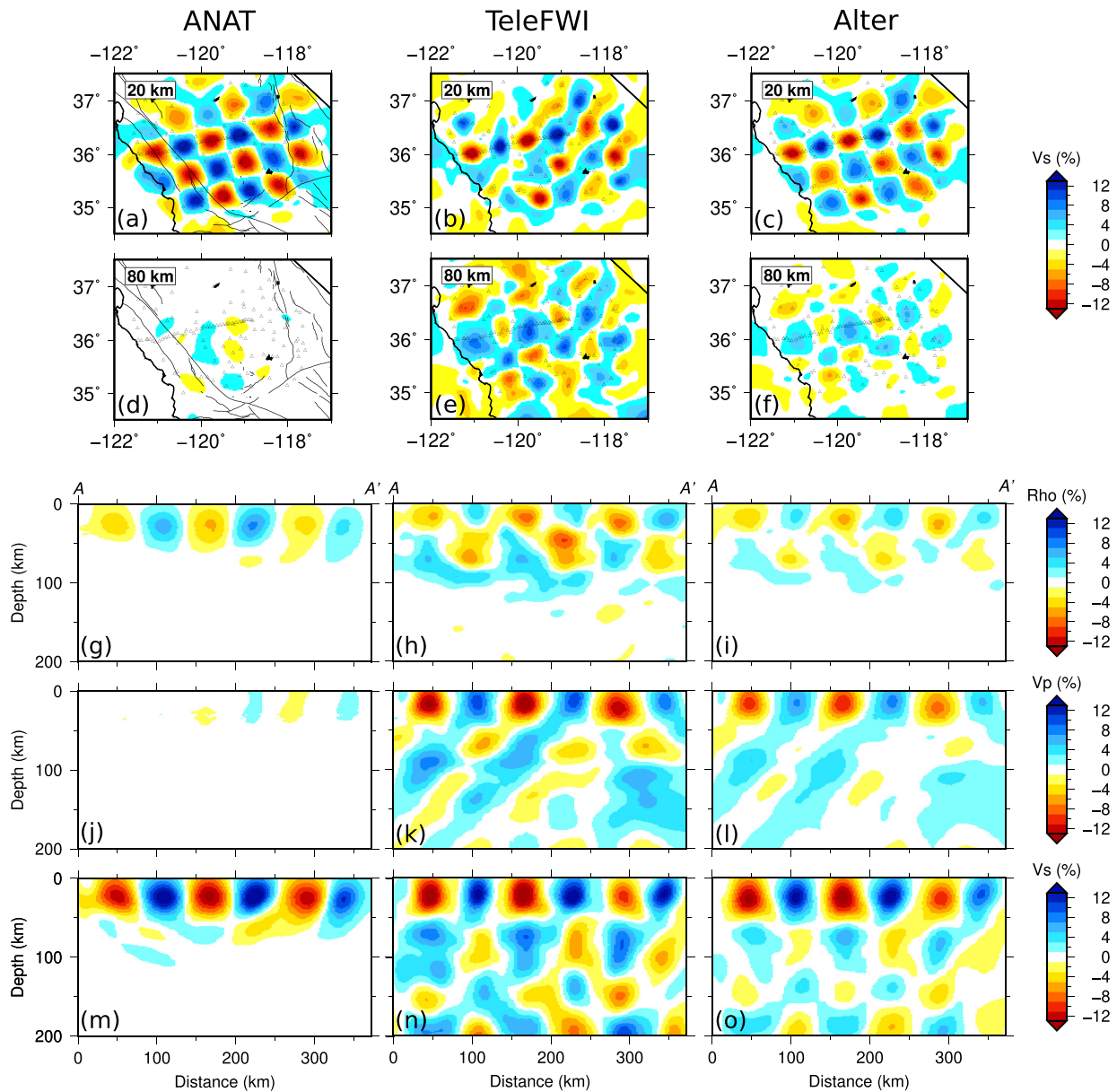


Figure 3. Recovered models of 40 km size 3D checkerboard tests for ANAT (left columns), TeleFWI (middle columns) and the alternating inversion (Alter, right columns). The top two rows exhibit the horizontal slices of V_s models at depths of (a–c) 20 km and (d–f) 80 km. The last three rows show the vertical cross-sections of (g–i) density, (j–l) V_p , and (m–o) V_s models beneath the AA' profile.

to V_s structures at shallow depths (Figure 3m, less than 60 km) which is limited by the frequency range of retrieved cross-correlations from ambient noise. Compared with ANAT, TeleFWI is sensitive to much deeper structures for all three model parameters (ρ , V_p , and V_s in Figure 3h, 3k, and 3n). However, it suffers from strong smearing shown in the horizontal cross-sections of the recovered models (Figures 3b and 3e) due to the near-vertical incidence of teleseismic P waves beneath the sparsely distributed receivers. Benefiting from the more uniform ray-path coverage between station pairs, surface waves help better illuminate structures at the off-line areas that are not well resolved in TeleFWI. Thus, the addition of surface waves in the alternating inversion helps alleviate the strong smearing at shallow depths (Figures 3c and 3f). At greater depths, the alternating inversion shares a similar resolution of the TeleFWI with slightly degraded amplitude recovery (Figure 3i, 3l, and 3o). These tests demonstrate that the alternating inversion combining the

complementary sensitivities of surface waves and teleseismic P waves is capable of building a more unified model, thus outperforming inversions based on individual data sets.

We further evaluate the model resolution based on synthetic tests using the TeleFWI scheme instead of the alternating inversion. Since alternating inversions are too computationally extensive for a series of synthetic models as shown latter, we use TeleFWI checkerboard test as a good approximation to the model resolution for the alternating inversion, except at shallow depths where additional checkerboard tests with a 40 km anomaly size have already been performed (Figure 3). The synthetic models are composed of a series of 3D checkerboard anomalies with sizes of 20, 40, and 80 km. In particular, two sets of anomaly distributions with different orientations are designed to specifically investigate the resolution along profiles AA' (Figures S3 and S4) and BB' (Figures S5 and S6), respectively. The results from these synthetic tests suggest that the resolution beneath the CCSE array for the Vs model decreases from 20 km at the top to 40 km at the bottom. As P waves have longer wavelengths than S waves, the Vp structure is less resolved in comparison with the Vs structure and the resolution is about 40 km in the upper 100 km and 80 km at greater depths. The resolution of the density is degraded from that of the Vs, and it can be only resolved in the upper 60 km. The resolutions of the three model parameters for the BB' profile are similar to those for the AA' profile. However, profile AA' shows slightly stronger smearing effects at depths below 50 km likely due to the existence of fewer stations north of the profile compared to those for BB'. Since the density and Vp models have limited resolution, we mainly focus our discussion on the Vs structures in this study.

3.4. Inversion Results

Figures 4a and 4b present the total misfit evolution of teleseismic P waveforms and ambient noise surface wave traveltimes respectively for the two separate inversions and the alternating inversion using real data sets. In general, the alternating inversion shows a slower convergence rate and slightly larger misfits than those from separate inversions. A similar pattern has also been seen in the traveltime joint inversion of Fang et al. (2016) which is reasonable as the alternating inversion scheme tries to fit both data sets simultaneously. The alternating inversion converges after 32 iterations when the misfit changes over the last iteration for both noise and teleseismic data are less than 3%. The final misfit reductions of the teleseismic (from 0.62 to 0.37) and ambient noise (from 1.77 to 0.90) data are about 40.3% and 49.2%, respectively. Figure 4c shows the differential traveltime histograms between EGFs and SGFs for the initial and final model from the alternating inversion. It is clear that this final model improves the data fitting significantly in comparison with the initial model, with a smaller overall average misfit and standard deviation (e.g., 0.85 ± 1.96 s to 0.12 ± 1.51 s). Examples of waveform fitting are also provided in Figures S7–S29.

To compare the results from the three types of inversions, we show their final Vs models at 15, 45, 75, and 110 km depths respectively in Figure 5. In general, the Vs images from ANAT agree well with the first-order velocity structures from previous tomographic studies (Bernardino et al., 2019; Jiang, Schmandt, Hansen, et al., 2018; Jones et al., 2014; Moschetti et al., 2010; Shen et al., 2013; Yang et al., 2008). For example, high velocities (+10%) referred to as the Foothills Anomaly (FA), are observed in the crust along the western foothills of Sierra Nevada Batholith (SNB), as also seen in the teleseismic P-wave tomography of Jones et al. (2014). Surrounding the FA, relatively low velocities are observed in the Great Valley (GV) (−3%), the eastern SNB and Walker Lane (WL) region (−6%). In the uppermost mantle (45 km), the whole SNB and WL region exhibit strong low velocities (−12%) while the western coast shows relatively high velocities. At this depth, ANAT also reveals a low velocity zone under the central GV that is not seen in previous surface wave tomography (Jiang, Schmandt, Hansen, et al., 2018; Shen et al., 2013). This anomaly might be influenced by the shallow thick sediments (<10 km) in GV which cannot be well constrained by ANAT due to the lack of short-period dispersion information. A similar fast-to-slow velocity feature from the coast to the northeast further extends to the depth of 75 km with smaller amplitudes, and almost no change of the Vs is obtained at greater depths (i.e., 110 km) due to degrading depth sensitivities of surface waves. Compared to ANAT, TeleFWI resolves similar Vs patterns in the crust but with smaller amplitudes. The major difference between the two models exists in the uppermost mantle where TeleFWI reveals a dominating high velocity body centered at 119.5°W and 36°N known as the Isabella Anomaly (IA) (e.g., Jones et al., 1994; Raikes, 1980). High velocities are also imaged beneath the central SNB in the lower crust and uppermost mantle in TeleFWI, which is contrary to low velocities observed by previous tomography studies (Bernardino et al., 2019; Jiang,

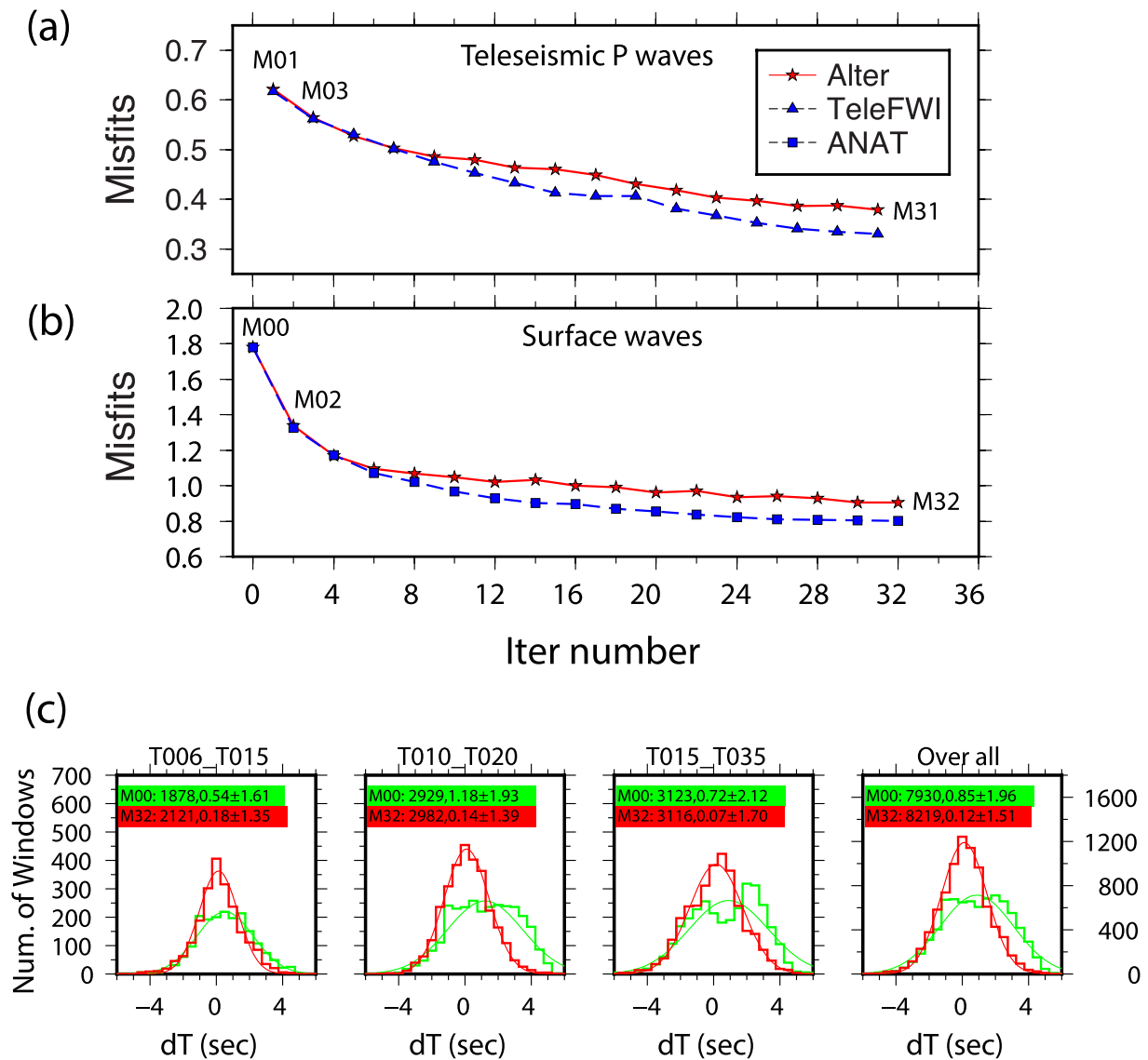


Figure 4. The total misfit evolution for (a) Teleseismic P waveforms and (b) Ambient noise surface waves over iterations in ANAT (blue rectangles), TeleFWI (blue triangles), and the alternating inversion (Alter, red stars). The alternating inversion starts from the smoothed AK135 model (M00), and alternatively fits surface wave (M00, M02, ..., etc) and body wave (M01, M03, ..., etc) data sets. Iteration numbers of ANAT and TeleFWI are multiplied by two to match those of the alternating inversion. (c) Differential traveltime histograms between EGFs and SGFs for the initial (green) and final (red) models at three periods bands, that is, 6–15 s, 10–20 s, 15–35 s for the alternating inversion. The histograms of overall misfits are shown in the last column.

Schmandt, Hansen, et al., 2018; Yang et al., 2008) in this area. The high velocities from TeleFWI may be an artifact caused by spatial aliasing effects resulting from the limited waveform data (Figures S26–S29). Moreover, TeleFWI reveals deeper Vs structures (e.g., 110 km) which are below the penetration depth of ANAT. The final Vs model from the alternating inversion accommodates the features from both ANAT and TeleFWI, including the three high velocity zones (FA, IA, and coastal high velocities) and the low velocity zone beneath the eastern SNB and WL.

In addition, we also show two vertical cross-sections (locations indicated in Figure 1a) of Vs structures to further examine the depth extent of the aforementioned velocity anomalies, particularly the FA and IA. The AA' profile (Figures 6a–6c) follows the dense linear array and extends eastward into the eastern SNB. In the ANAT model, the coastal high velocity body is observed to dip sub-horizontally eastward with an overriding wedge-like low velocity zone beneath the central GV. Under the western SNB, the high velocity FA (+10%)

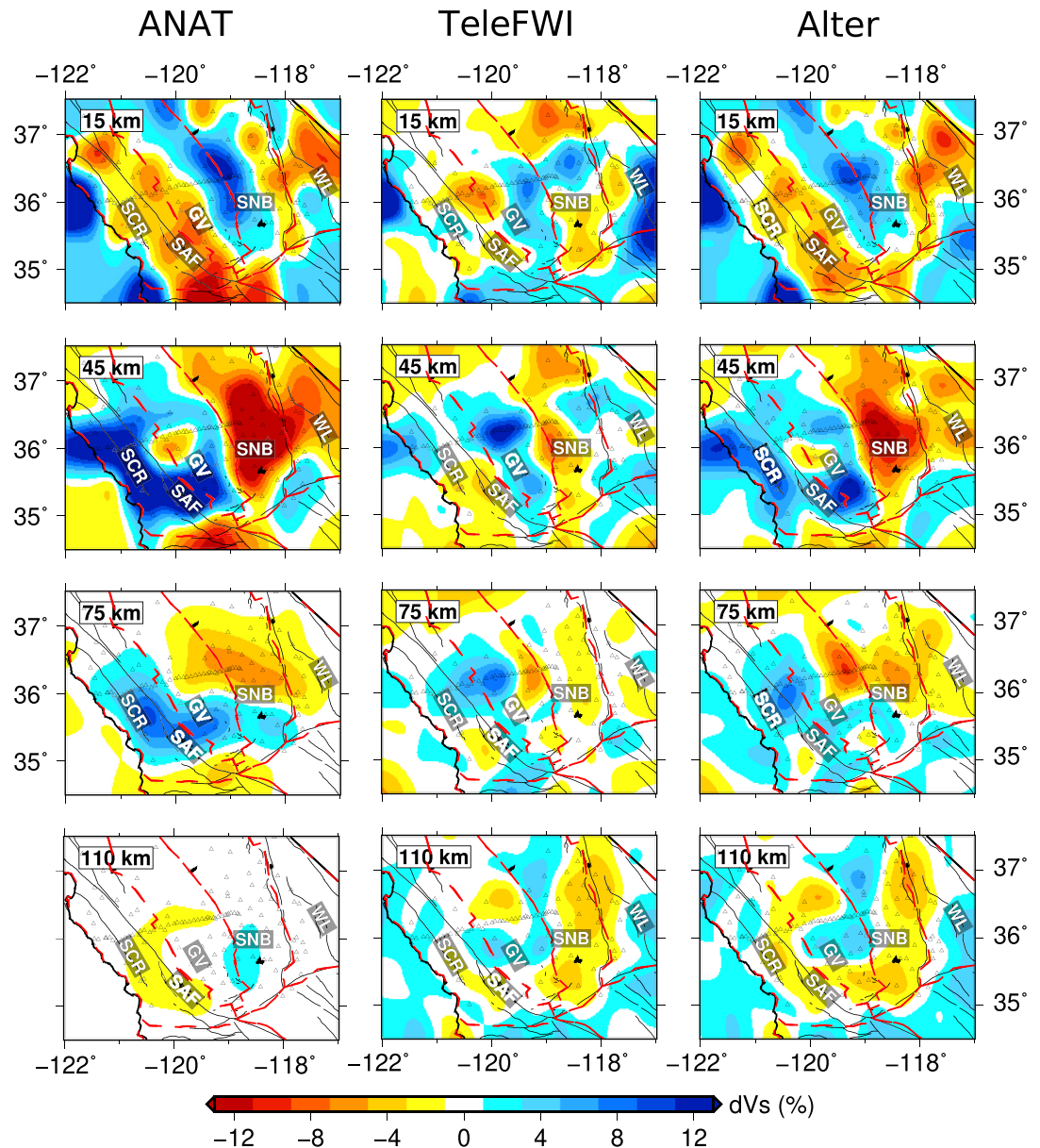


Figure 5. Horizontal slices of Vs images from ANAT (left columns), TeleFWI (middle columns) and the alternating inversion (right columns) at depths of 15, 45, 75, and 110 km.

is mostly confined to the upper 50 km, while low velocities (-12%) show up at greater depths that extend upward to the east toward the eastern SNB (Figure 6a). In comparison, TeleFWI only reveals a weak (-4%) east-dipping coastal high velocity body and the strong low velocities (-12%) beneath GV is mostly confined to the shallow crust. The high velocity features identified in the upper mantle as IA1 seems to be connected to the shallow FA, in company with a strip-like low velocity body below (Figure 6b). We notice that there are some discrepancies between the Vs images from the ANAT and TeleFWI beneath the GV and SNB at depths of 30–70 km, which are mainly due to the different data sensitivities and coverage of ANAT and TeleFWI. The alternating inversion (Figure 6c) eventually reveals high velocities beneath the GV and low velocities below the SNB in the lower crust and uppermost mantle, which is more reasonable and consistent with previous tomographic models based on large traveltime data sets (Bernardino et al., 2019; Jiang, Schmandt, Hansen, et al., 2018; Yang et al., 2008) compared with results from the two separate inversions. The final model shows the three high Vs bodies (coastal high velocities, IA1 and FA) are connected and also shows

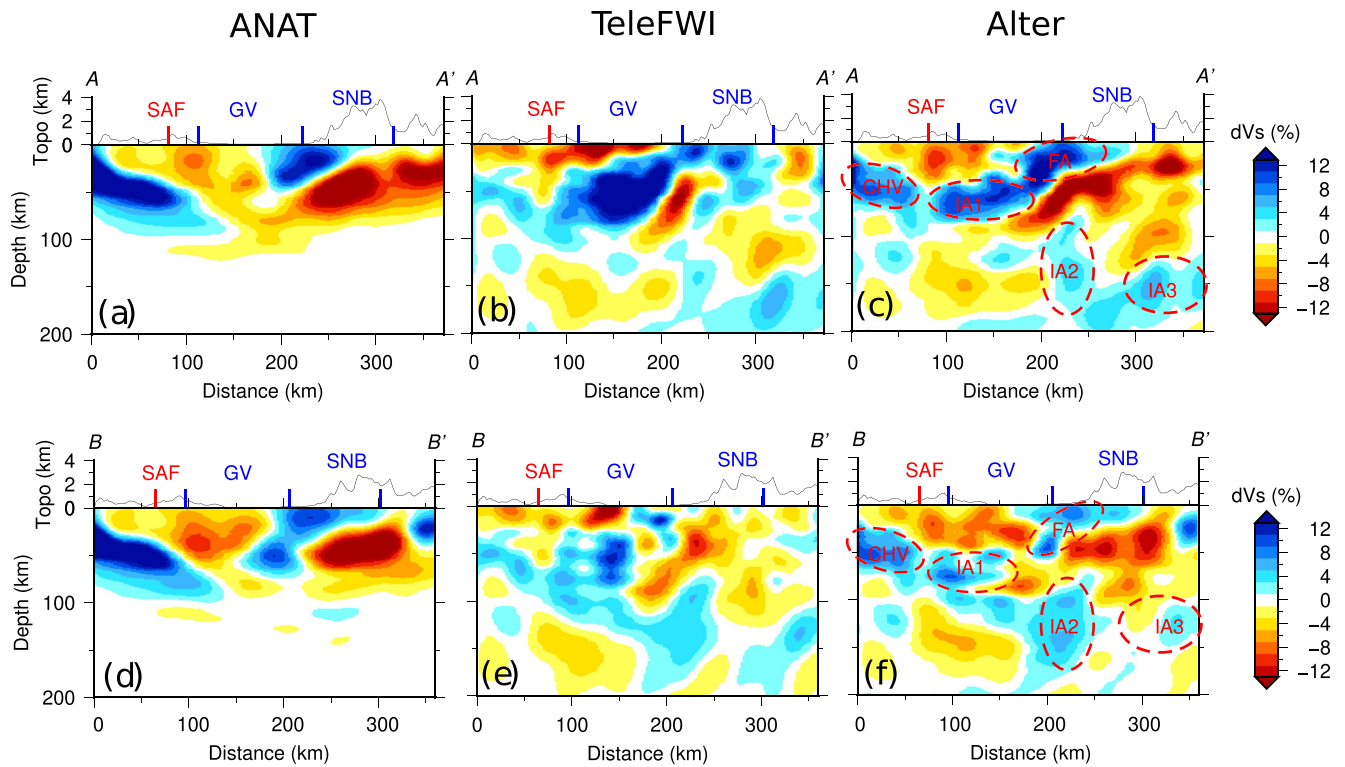


Figure 6. Vertical cross-sections (a–c) AA' and (d–f) BB' of Vs images from the ANAT (a, d), TeleFWI (b, e), and alternating (c, f) inversions. High Vs zones: CHV-Coastal High Velocities; IA-Isabella Anomaly; FA-Foothills Anomaly.

the low velocities beneath the SNB are merged to form an oblique low velocity zone from the eastern SNB to below IA1. At greater depths, two high Vs bodies (IA2 and IA3) are imaged beneath the SNB and may be interpreted as the deeper parts of the IA (Bernardino et al., 2019; Wang et al., 2013).

Another profile (BB') along the latitude 36°N is shown to facilitate model comparisons with previous tomography models (Bernardino et al., 2019; Jiang, Schmandt, Hansen, et al., 2018; Jones et al., 2014; Yang et al., 2008). In general, the velocity variations along this profile is similar to those along AA' in the top 80 km. The amplitudes of the velocity anomalies from TeleFWI decrease from the profile AA' to BB', probably due to coarser station intervals off-line of the dense CCSE array. The major feature seen in BB' that differs from AA' is that the IA1 is connected with the deeper IA2 instead of the shallow FA.

4. Discussions

4.1. Model Comparison and Implications

Central California is located in a tectonically complex region where the lithospheric structures are shaped by a prolonged tectonic history involving slab subduction, plate boundary transformation and associated mantle dynamics. Previous tomographic studies (e.g., Bernardino et al., 2019; Boyd et al., 2004; Jones et al., 1994, 2014; Jiang, Schmandt, Hansen, et al., 2018; Yang et al., 2008; Zandt et al., 2004) have provided valuable information on the seismic structures of this region. However, the resolution of previous tomographic studies in the upper mantle is limited to about 60 km or larger. In this section, we compare the velocity models of central California from our alternating inversion with those from traditional ray-theory based methods to demonstrate the feasibility and advantage of our method in practical tomography. In particular, we focus on some interesting small-scale features revealed in our model that are beyond the resolution of traditional methods, and discuss their associated tectonic implications.

Figure 7 shows the comparison of seismic features seen in our final Vs model with (a) the interfaces inferred from common conversion-point (CCP) image of Sp receiver functions by Hoots (2016) and (b) the Vs

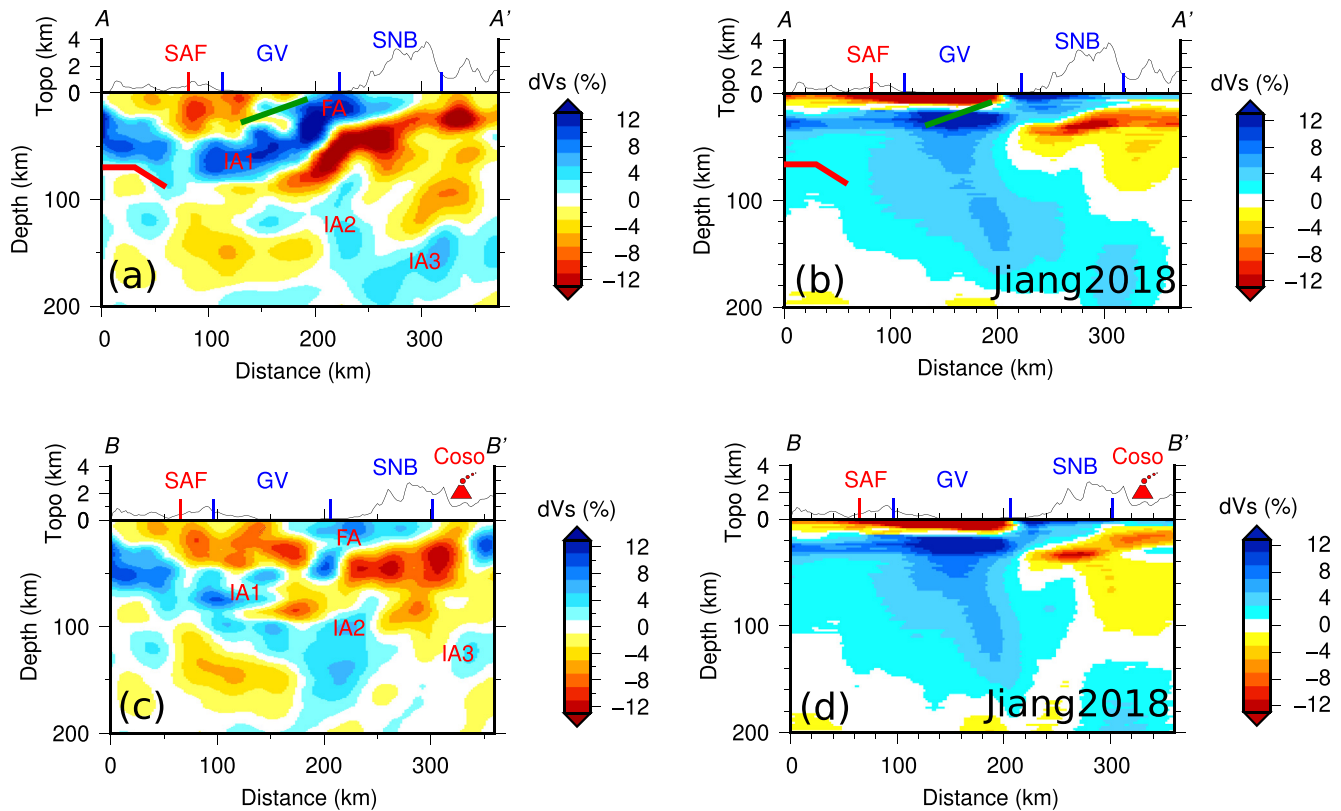


Figure 7. Comparison of Vs images along profiles (a–b) AA' and (c–d) BB' from this study and the one from Rayleigh wave tomography (Jiang2018) by Jiang, Schmandt, Hansen, et al. (2018). The thick green and red lines in (a) and (b) denote the velocity contrasts from Sp receiver function (Hoots, 2016).

model from surface wave tomography based on ambient noise and teleseismic surface wave data by Jiang, Schmandt, Hansen, et al. (2018), hereafter called Jiang2018 model. Our new Vs model shows drastically better coincidence with interface structures revealed by the receiver function study of Hoots (2016) compared to the Jiang2018 model due to the consideration of scattered wave energy within TeleFWI, clearly illustrated at two regions with receiver function results. First, at the west end of the two cross-sections, a prominent high velocity anomaly is observed in the lithosphere and dips to the east reaching ~100 km depth beneath the SAF. This feature exhibits a similar pattern in profiles AA' and BB' and its bottom depth is consistent with the lithosphere-asthenosphere boundary (LAB) identified by the Sp receiver function analysis of Hoots (2016). This boundary has been interpreted as the base of the oceanic Monterey microplate (Hoots, 2016) and the dipping geometry of this high velocity anomaly from our model generally agrees with this interpretation. At the conjunction area between the GV and the western SNB, we observe another interesting velocity contrast with low Vs beneath the central GV and west-dipping high Vs beneath the Sierran foothills (Figures 7a and 6b). This feature is generally consistent with the transition of positive to negative velocity gradient (green line in Figure 7a) observed in the Sp receiver function study (Hoots, 2016) as well as the recent P-wave receiver function study (Dougherty et al., 2020).

In addition to the improvement of interface structures, our model also reveals finer Vs structures in the upper mantle compared with the Jiang2018 model. For example, the well-known high velocity IA has a thickness of ~100 km shown in the profiles of AA' and BB' based on the Jiang2018 model, while the IA in our model has a thickness of about 40 km. The Jiang2018 model is inverted from frequency-dependent dispersion curves of surface waves which are mostly sensitive to smoothly varying velocities but place very weak constraints on interface structures, making it hard to infer the accurate thickness of the high velocity body in their study. In contrast, TeleFWI used in our alternating inversion enables us to image smaller-scale heterogeneities (40 km as shown in Figure 3) and sharp velocity discontinuities, resulting in a more concentrated and thinner high velocity anomaly for IA.

The geometry of the IA provides a piece of key observational evidence in deciphering its origin as either being the foundering lithosphere (e.g., Boyd et al., 2004; Zandt et al., 2004) beneath the southern SNB or representing a fossil slab connected to the Monterey microplate (e.g., Jiang, Schmandt, Hansen, et al., 2018; Wang et al., 2013). In the Jiang2018 model, the high velocity anomaly dips continuously eastward from the coast to the depth of 200 km beneath the eastern SNB, and is regarded as direct evidence of the fossil slab mechanism. However in our model, this anomaly is truncated at about 100 km by a westward-dipping low V_s body beneath the SNB, separating the shallow IA1 from the deeper IA2 and IA3 beneath the SNB (Figure 7a). There are also considerable differences in the geometry of this low velocity anomaly between profiles AA' and BB'. Along the BB' profile (Figure 7c), the low V_s is relatively weak and the deeper IA2 seems to be attached to the IA1 to form a continuous eastward dipping high velocity body. Due to the small number of stations used in previous teleseismic P tomography (Boyd et al., 2004; Jones et al., 2014; Zandt et al., 2004) in the west of the foothills and GV, the IA is revealed as a sub-vertical high velocity anomaly, and its proximity to low velocities beneath the SNB further contributes to the interpretation of being the delaminated lithosphere from the eastern SNB. With the new data from the CCSE array as well as the newly implemented alternating inversion method, our new model suggests that the shallow IA1 is more likely to be part of the subducted oceanic slab rather than a foundering lithosphere from the SNB. The high velocity slab dips eastward to the depth of at least 100 km beneath the eastern GV, and possibly has a connection with the deeper high velocity anomalies beneath the SNB. The model also reveals possible velocity gaps along the projected trend of the oceanic slab, suggesting that the subducted slab may break off from the western part. The velocity gap may be a localized small-scale feature, which is below the resolution outside the dense CCSE line. To completely constrain the full picture of the 3D geometry of the IA, future deployments of denser stations with more data sets in the off-line region may be needed.

4.2. Limitations and Future Perspectives

In this study, we have demonstrated the advantage of the alternating inversion over individual inversions of surface waves and teleseismic P waves through a series of 3D synthetic tests and an application to seismic data recorded in central California. More specifically, TeleFWI has high resolution in the vicinity of the dense array and can reveal small-scale heterogeneities and constrain sharp velocity boundaries (such as the Moho and LAB) in the upper mantle, while ANAT using broadly distributed stations has relatively uniform ray coverage with a good lateral resolution for V_s structures in the crust and uppermost mantle. The alternating inversion enables the construction of a more unified model by combining the sensitivities of surface wave and body wave data. In the following, we discuss several aspects of the alternating inversion that may be considered for improvement in future studies.

First, the FK-SEM hybrid method adopted in TeleFWI is based on a plane wave assumption which does not consider the spherical curvature of the Earth. To overcome this limitation, the external 1D solver outside the target area in hybrid methods needs to be replaced by 1D efficient global solvers for a spherical Earth model, such as those based on normal modes (Capdeville et al., 2003), direct solution method (DSM, e.g., Monteiller et al., 2013, 2015), and axisymmetric SEM (AxiSEM, e.g., Beller, Monteiller, Operto, et al., 2018). Nevertheless, it is worth noting that the forward simulation of the FK-SEM hybrid method is much faster than the other global hybrid methods mentioned above, and it is sufficiently accurate for modeling teleseismic wavefields when the array aperture is much smaller than epicenter distances (Monteiller et al., 2020).

Second, the ANAT method used in the alternating inversion does not consider effects of uneven distributed noise sources and data processing on the Green's function retrieval (Fichtner, 2014; Fichtner et al., 2020; Froment et al., 2010; Luo et al., 2020; Tsai, 2009; Wang, Luo, & Yang, 2016; Yao & Van Der Hilst, 2009) and source-structure tradeoffs (Fichtner, 2015; Sager et al., 2018; Tromp et al., 2010). Although time shifts measured in narrow bands are less prone to misfit biases resulting from inhomogeneous noise sources and data processing, full-waveform inversions of noise correlations that fail to account for these effects could introduce tomographic artifacts and hardly controllable source-structure tradeoffs (Fichtner, 2014, 2015). The FWANI technique (Sager et al., 2018, 2020) jointly inverts for the noise source distribution and Earth structure, providing an promising approach to reduce source-structure tradeoffs by completely exploiting waveform information from both positive and negative components of noise correlations. More recently, Fichtner et al. (2020) advocate optimal processing schemes to further reduce nonphysical components

introduced into noise correlations by data processing, such as time and frequency domain normalization (Bensen et al., 2007). These significant advances in noise interferometry will contribute to more robust waveform-based ambient noise tomographic images, which are desired to be incorporated into future alternating inversions.

Third, the performance of the alternating inversion is determined by the complementary constraints from the two different data sets. For a specific region in the model, there are generally three different scenarios regarding data sensitivities and resulting model updates: (a) one of the two datasets has no/little sensitivities; (b) both datasets has sensitivities and generate model updates that are consistent with each other; (c) both datasets have sensitivities but generate significant discrepancies between their model updates. In areas where depths >100 km (Case 1) and most shallow regions (Case 2), the two data sets used in this study are complementary to each other and the alternating inversion contributes to a constructive model improvement. This is evidenced by large misfit reductions for both data sets in the alternating inversion in Figures 4a and 4b. In Case 3, such as the areas beneath the GV and SNB, the model updates from the two data sets are in opposite directions. Consequently, the model changes from the alternating inversion beneath these areas are oscillatory and do not converge to a unique stationary solution, resulting in the degradation of waveform fitting for both data sets in comparison with those from separate inversions (Figures 4a and 4b). In this case, the final Vs model from our alternating inversion method represents the average velocity structure constrained by the two data sets, which is accepted in this study because it is more consistent with previous studies than those from separate inversions (Section 3.4). In the future, the model update for such regions can be potentially improved by adopting weighting schemes to further adjust misfit contributions from different data sets, or starting with a misfit objective function that includes explicit regularization parameters. Moreover, it would be beneficial to further improve the inversion result of TeleFWI at deep depths (>100 km) by adding more data sets sampling the off-line areas. One significant advantage of adjoint tomography is that the model can continue to be updated whenever new data sets become available. Compared with the relatively scarce high-quality waveforms of scattered waves, there are a large number of traveltimes data for other primary seismic phases such as direct P/S, PKP/SKS, etc. Traveltime adjoint tomography of other primary phases could also be included in future alternating inversions to further improve the resolution of the Vp and Vs images of the lithospheric mantle.

5. Conclusion

In this study, we propose an alternating inversion scheme that fits ambient noise surface waves and teleseismic P waves simultaneously based on 3D seismic wave simulations. The method is applied to ambient noise empirical Green's functions from 60 virtual sources, direct P and scattered waves from 11 teleseismic events in the central California plate boundary region. By comparing the tomographic results from ambient noise adjoint tomography, teleseismic full-waveform inversion and the alternating inversion using both field data sets and synthetics from 3D checkerboard models, we demonstrate that the alternating inversion outperforms separate inversions as it combines the complementary sensitivities of both toward a more unified model. The final Vs model from our alternating inversion delineates a distinct interface between the GV and western SNB in the crust and the LAB underneath the western coast, which are in good agreement with recent receiver function studies. Furthermore, the new model also reveals a refined geometry of the high velocity Isabella Anomaly with a thickness of about 40 km. The shallow Isabella Anomaly is part of the subducted oceanic slab which dips eastward to at least 100 km depth beneath the eastern GV and possibly breaks off at greater depths. This proposed alternating inversion scheme can be applied to other regions with both a dense linear array and regional array networks to obtain high-resolution lithospheric images. Additional phases and wavefields can be further incorporated using a similar inversion framework.

Appendix A: Teleseismic Traveltime Estimation for FK-SEM

The traveltime delay from the initial wavefront through (x_0, y_0, z_0) to a surface point at $(x_r, y_r, 0)$ can be calculated as:

$$T_r^{FK} = p[(x_r - x_0)\cos\phi + (y_r - y_0)\sin\phi] + \eta_0 * (z_{bot} - z_0) + \sum_{m=1}^n \eta_m * H_m, \quad (A1)$$

where

$$p = \frac{\sin\theta}{v_0}; \eta_m = \sqrt{\frac{1}{v_m^2} - p^2} \quad (A2)$$

In above, ϕ is the azimuth, H_m is the thickness of the m 'th layer. z_{bot} is the z coordinate of the bottom of all layers (top of half space). p is the horizontal slowness (ray parameter) which is conserved along the ray and θ is the incident angle. v_m is the P or S wave velocity in m 'th layer and the corresponding vertical slowness is η_m . Note $m = 0$ indicates the velocity/slowness in the halfspace.

Data Availability Statement

The seismic data used in this study are downloaded from the Caltech/USGS Southern California Seismic Network (<https://doi.org/10.7914/SN/CI>) and IRIS DMC (<https://ds.iris.edu/ds/nodes/dmc/>). The open source spectral-element software package SPECFEM3D Cartesian used in this study are freely available for download via the Computational Infrastructure for Geodynamics (CIG; geodynamics.org). The FWAT package developed in this study can be downloaded from <http://doi.org/10.5281/zenodo.4747811>.

Acknowledgments

The authors thank the Editor Michael Bostock for handling this manuscript, the Associate Editor Andreas Fichtner and two anonymous reviewers for their constructive suggestions that have improved the manuscript significantly. Computations for this study were performed on hardware acquired through the combined funding of Canada Foundation for Innovation (CFI), Ontario Research Fund (ORF), and University of Toronto Startup Fund and partly hosted by the SciNet HPC Consortium. K. Wang (after January 2020) and Y. Yang are supported by the Australian Research Council Discovery Grants DP190102940. K. Wang (before January 2020) and Q. Liu are supported by the NSERC Discovery Grant 487237. This is contribution 1664 from the ARC Center of Excellence for Core to Crust Fluid Systems and 1465 in the GEMOC Key Center.

References

- Aki, K., Christofferson, A., & Husebye, E. S. (1976). Three-dimensional seismic structure of the lithosphere under Montana LISA. *Bulletin of the Seismological Society of America*, 66(2), 501–524.
- Beller, S., Monteiller, V., Combe, L., Operto, S., & Nolet, G. (2018). On the sensitivity of teleseismic full-waveform inversion to earth parameterization, initial model and acquisition design. *Geophysical Journal International*, 212(2), 1344–1368. <https://doi.org/10.1093/gji/ggx480>
- Beller, S., Monteiller, V., Operto, S., Nolet, G., Paul, A., & Zhao, L. (2018). Lithospheric architecture of the South-Western Alps revealed by multiparameter teleseismic full-waveform inversion. *Geophysical Journal International*, 212(2), 1369–1388. <https://doi.org/10.1093/gji/ggx216>
- Bensen, G., Ritzwoller, M., Barmin, M., Levshin, A. L., Lin, F., Moschetti, M., et al. (2007). Processing seismic ambient noise data to obtain reliable broad-band surface wave dispersion measurements. *Geophysical Journal International*, 169(3), 1239–1260. <https://doi.org/10.1111/j.1365-246x.2007.03374.x>
- Bensen, G., Ritzwoller, M., & Shapiro, N. M. (2008). Broadband ambient noise surface wave tomography across the United States. *Journal of Geophysical Research*, 113(B5). <https://doi.org/10.1029/2007jb005248>
- Bernardino, M. V., Jones, C. H., Levandowski, W., Bastow, I., Owens, T. J., & Gilbert, H. (2019). A multicomponent Isabella anomaly: Resolving the physical state of the Sierra Nevada upper mantle from Vp/Vs anisotropy tomography. *Geosphere*, 15(6), 2018–2042. <https://doi.org/10.1130/ges02093.1>
- Bostock, M. (2004). Green's functions, source signatures, and the normalization of teleseismic wave fields. *Journal of Geophysical Research*, 109(B3). <https://doi.org/10.1029/2003jb002783>
- Boyd, O. S., Jones, C. H., & Sheehan, A. F. (2004). Foundering lithosphere imaged beneath the southern Sierra Nevada, California, USA. *Science*, 305(5684), 660–662. <https://doi.org/10.1126/science.1099181>
- Bozdağ, E., Peter, D., Lefebvre, M., Komatitsch, D., Tromp, J., Hill, J., et al. (2016). Global adjoint tomography: First-generation model. *Geophysical Journal International*, 207(3), 1739–1766.
- Capdeville, Y., Chaljub, E., Vilotte, J. P., & Montagner, J. P. (2003). Coupling the spectral element method with a modal solution for elastic wave propagation in global earth models. *Geophysical Journal International*, 152(1), 34–67. <https://doi.org/10.1046/j.1365-246x.2003.01808.x>
- Chen, M., Huang, H., Yao, H., Hilst, R., & Niu, F. (2014). Low wave speed zones in the crust beneath SE Tibet revealed by ambient noise adjoint tomography. *Geophysical Research Letters*, 41(2), 334–340. <https://doi.org/10.1002/2013gl058476>
- Chen, M., Niu, F., Liu, Q., Tromp, J., & Zheng, X. (2015). Multiparameter adjoint tomography of the crust and upper mantle beneath East Asia: 1. Model construction and comparisons. *Journal of Geophysical Research: Solid Earth*, 120(3), 1762–1786. <https://doi.org/10.1002/2014jb011638>
- Dougherty, S. L., Jiang, C., Clayton, R. W., Schmandt, B., & Hansen, S. M. (2020). Seismic evidence for a fossil slab origin for the Isabella anomaly. *Geophysical Journal International*, 224(2), 1188–1196. <https://doi.org/10.1093/gji/ggaa472>
- Ekström, G., Tromp, J., & Larson, E. W. (1997). Measurements and global models of surface wave propagation. *Journal of Geophysical Research*, 102(B4), 8137–8157. <https://doi.org/10.1029/96jb03729>
- Ermert, L., Sager, K., Afanasiev, M., Boehm, C., & Fichtner, A. (2017). Ambient seismic source inversion in a heterogeneous earth: Theory and application to the Earth's hum. *Journal of Geophysical Research: Solid Earth*, 122(11), 9184–9207. <https://doi.org/10.1002/2017jb014738>
- Fang, H., Zhang, H., Yao, H., Allam, A., Zigone, D., Ben-Zion, Y., et al. (2016). A new algorithm for three-dimensional joint inversion of body wave and surface wave data and its application to the Southern California plate boundary region. *Journal of Geophysical Research: Solid Earth*, 121(5), 3557–3569. <https://doi.org/10.1002/2015jb012702>
- Fichtner, A. (2014). Source and processing effects on noise correlations. *Geophysical Journal International*, 197(3), 1527–1531. <https://doi.org/10.1093/gji/ggu093>

- Fichtner, A. (2015). Source-structure trade-offs in ambient noise correlations. *Geophysical Journal International*, 202(1), 678–694. <https://doi.org/10.1093/gji/ggv182>
- Fichtner, A., Bowden, D., & Ermert, L. (2020). Optimal processing for seismic noise correlations. *Geophysical Journal International*, 223(3), 1548–1564. <https://doi.org/10.1093/gji/ggaa390>
- Fichtner, A., Kennett, B. L., Igel, H., & Bunge, H.-P. (2009). Full seismic waveform tomography for upper-mantle structure in the Australasian region using adjoint methods. *Geophysical Journal International*, 179(3), 1703–1725. <https://doi.org/10.1111/j.1365-246x.2009.04368.x>
- Friederich, W. (2003). The S-velocity structure of the East Asian mantle from inversion of shear and surface waveforms. *Geophysical Journal International*, 153(1), 88–102. <https://doi.org/10.1046/j.1365-246x.2003.01869.x>
- Froment, B., Campillo, M., Roux, P., Gouédard, P., Verdel, A., & Weaver, R. L. (2010). Estimation of the effect of nonisotropically distributed energy on the apparent arrival time in correlations. *Geophysics*, 75(5), SA85–SA93. <https://doi.org/10.1190/1.3483102>
- Gao, H., & Shen, Y. (2014). Upper mantle structure of the Cascades from full-wave ambient noise tomography: Evidence for 3D mantle upwelling in the back-arc. *Earth and Planetary Science Letters*, 390, 222–233. <https://doi.org/10.1016/j.epsl.2014.01.012>
- Guo, Z., Wang, K., Yang, Y., Tang, Y., John Chen, Y., & Hung, S.-H. (2018). The origin and mantle dynamics of quaternary intraplate volcanism in Northeast China from joint inversion of surface wave and body wave. *Journal of Geophysical Research: Solid Earth*, 123(3), 2410–2425. <https://doi.org/10.1002/2017jb014948>
- Halldor, B., & Venegas, S. A. (1997). *A manual for EOF and SVD analyses of climate data, CCGCR Report* (Vols. 97–1, p. 52). McGill University.
- Hoots, C. (2016). *Seismic imaging of the lithosphere-asthenosphere boundary with a dense broadband array in central California (Unpublished master's thesis)*. University of New Mexico.
- Hung, S.-H., Shen, Y., & Chiao, L.-Y. (2004). Imaging seismic velocity structure beneath the Iceland hot spot: A finite frequency approach. *Journal of Geophysical Research*, 109(B8). <https://doi.org/10.1029/2003jb002889>
- Jiang, C., & Denolle, M. A. (2020). NoisePy: A new high-performance python tool for ambient-noise seismology. *Seismological Research Letters*, 91(3), 1853–1866. <https://doi.org/10.1785/0220190364>
- Jiang, C., Schmandt, B., Hansen, S. M., Dougherty, S. L., Clayton, R. W., Farrell, J., & Lin, F.-C. (2018). Rayleigh and S wave tomography constraints on subduction termination and lithospheric foundering in central California. *Earth and Planetary Science Letters*, 488, 14–26. <https://doi.org/10.1016/j.epsl.2018.02.009>
- Jiang, C., Schmandt, B., Ward, K. M., Lin, F.-C., & Worthington, L. L. (2018). Upper mantle seismic structure of Alaska from Rayleigh and S wave tomography. *Geophysical Research Letters*, 45(19), 10–350. <https://doi.org/10.1029/2018gl079406>
- Jones, C. H., Kanamori, H., & Roecker, S. W. (1994). Missing roots and mantle “drips”: Regional Pn and teleseismic arrival times in the southern Sierra Nevada and vicinity, California. *Journal of Geophysical Research*, 99(B3), 4567–4601. <https://doi.org/10.1029/93jb01232>
- Jones, C. H., Reeg, H., Zandt, G., Gilbert, H., Owens, T. J., & Stachnik, J. (2014). P-wave tomography of potential convective downwellings and their source regions, Sierra Nevada, California. *Geosphere*, 10(3), 505–533. <https://doi.org/10.1130/ges00961.1>
- Kennett, B. L., Engdahl, E., & Buland, R. (1995). Constraints on seismic velocities in the Earth from traveltimes. *Geophysical Journal International*, 122(1), 108–124. <https://doi.org/10.1111/j.1365-246x.1995.tb03540.x>
- Kikuchi, M., & Kanamori, H. (1982). Inversion of complex body waves. *Bulletin of the Seismological Society of America*, 72(2), 491–506.
- Komatitsch, D., & Vilotte, J.-P. (1998). The spectral element method: An efficient tool to simulate the seismic response of 2D and 3D geological structures. *Bulletin of the Seismological Society of America*, 88(2), 368–392.
- Krischer, L., Fichtner, A., Boehm, C., & Igel, H. (2018). Automated large-scale full seismic waveform inversion for North America and the North Atlantic. *Journal of Geophysical Research: Solid Earth*, 123(7), 5902–5928. <https://doi.org/10.1029/2017jb015289>
- Lay, T., Kanamori, H., Ammon, C. J., Hutko, A. R., Furlong, K., & Rivera, L. (2009). The 2006–2007 Kuril Islands great earthquake sequence. *Journal of Geophysical Research*, 114(B11). <https://doi.org/10.1029/2008jb006280>
- Lin, C., Monteiller, V., Wang, K., Liu, T., Tong, P., & Liu, Q. (2019). High-frequency seismic wave modeling of the deep Earth based on hybrid methods and spectral-element simulations: A conceptual study. *Geophysical Journal International*, 219(3), 1948–1969. <https://doi.org/10.1093/gji/ggz413>
- Lin, F.-C., Ritzwoller, M. H., Townend, J., Bannister, S., & Savage, M. K. (2007). Ambient noise Rayleigh wave tomography of New Zealand. *Geophysical Journal International*, 170(2), 649–666. <https://doi.org/10.1111/j.1365-246x.2007.03414.x>
- Liu, Q., & Gu, Y. (2012). Seismic imaging: From classical to adjoint tomography. *Tectonophysics*, 566, 31–66. <https://doi.org/10.1016/j.tecto.2012.07.006>
- Liu, Q., & Tromp, J. (2006). Finite-frequency kernels based on adjoint methods. *Bulletin of the Seismological Society of America*, 96(6), 2383–2397. <https://doi.org/10.1785/0120060041>
- Lloyd, A., Wiens, D., Zhu, H., Tromp, J., Nyblade, A., Aster, R., et al. (2020). Seismic structure of the Antarctic upper mantle imaged with adjoint tomography. *Journal of Geophysical Research: Solid Earth*, 125(3). <https://doi.org/10.1029/2019jb017823>
- Lou, X., Van Der Lee, S., & Lloyd, S. (2013). AIMBAT: A Python/Matplotlib tool for measuring teleseismic arrival times. *Seismological Research Letters*, 84(1), 85–93. <https://doi.org/10.1785/0220120033>
- Lu, Y., Stehly, L., Brossier, R., Paul, A., & Group, A. W. (2020). Imaging Alpine crust using ambient noise wave-equation tomography. *Geophysical Journal International*, 222(1), 69–85. <https://doi.org/10.1093/gji/ggaa145>
- Luo, Y., Yang, Y., Xie, J., Yang, X., Ren, F., Zhao, K., & Xu, H. (2020). Evaluating uncertainties of phase velocity measurements from cross-correlations of ambient seismic noise. *Seismological Research Letters*, 91(3), 1717–1729. <https://doi.org/10.1785/0220190308>
- Masson, Y., & Romanowicz, B. (2016). Fast computation of synthetic seismograms within a medium containing remote localized perturbations: A numerical solution to the scattering problem. *Geophysical Journal International*, 208(2), 674–692. <https://doi.org/10.1093/gji/ggw412>
- Monteiller, V., Beller, S., Plazolles, B., & Chevrot, S. (2020). On the validity of the planar wave approximation to compute synthetic seismograms of teleseismic body waves in a 3-D regional model. *Geophysical Journal International*, 224(3) 2060–2076.
- Monteiller, V., Chevrot, S., Komatitsch, D., & Fuji, N. (2013). A hybrid method to compute short-period synthetic seismograms of teleseismic body waves in a 3-D regional model. *Geophysical Journal International*, 192(1), 230–247. <https://doi.org/10.1093/gji/ggs006>
- Monteiller, V., Chevrot, S., Komatitsch, D., & Wang, Y. (2015). Three-dimensional full waveform inversion of short-period teleseismic wavefields based upon the SEM-DSM hybrid method. *Geophysical Journal International*, 202(2), 811–827. <https://doi.org/10.1093/gji/ggv189>
- Montelli, R., Nolet, G., Dahlen, F., Masters, G., Engdahl, E. R., & Hung, S.-H. (2004). Finite-frequency tomography reveals a variety of plumes in the mantle. *Science*, 303(5656), 338–343. <https://doi.org/10.1126/science.1092485>
- Moschetti, M., Ritzwoller, M., Lin, F.-C., & Yang, Y. (2010). Crustal shear wave velocity structure of the western United States inferred from ambient seismic noise and earthquake data. *Journal of Geophysical Research: Solid Earth*, 115(B10). <https://doi.org/10.1029/2010jb007448>

- Nocedal, J., & Wright, S. (2006). *Numerical optimization*. Springer Science & Business Media.
- Nunn, C., Roecker, S. W., Priestley, K. F., Liang, X., & Gilligan, A. (2014). Joint inversion of surface waves and teleseismic body waves across the Tibetan collision zone: The fate of subducted Indian lithosphere. *Geophysical Journal International*, 198(3), 1526–1542. <https://doi.org/10.1093/gji/ggu193>
- Obrebski, M., Allen, R. M., Pollitz, F., & Hung, S.-H. (2011). Lithosphere-asthenosphere interaction beneath the western United States from the joint inversion of body-wave traveltimes and surface-wave phase velocities. *Geophysical Journal International*, 185(2), 1003–1021. <https://doi.org/10.1111/j.1365-246x.2011.04990.x>
- Owens, T. J., Crotwell, H. P., Groves, C., & Oliver-Paul, P. (2004). SOD: Standing order for data. *Seismological Research Letters*, 75(4), 515–520. <https://doi.org/10.1785/gssrl.75.4.515-a>
- Peter, D., Komatitsch, D., Luo, Y., Martin, R., Le Goff, N., Casarotti, E., et al. (2011). Forward and adjoint simulations of seismic wave propagation on fully unstructured hexahedral meshes. *Geophysical Journal International*, 186(2), 721–739. <https://doi.org/10.1111/j.1365-246x.2011.05044.x>
- Pienkowska, M., Monteiller, V., & Nissen-Meyer, T. (2020). High-frequency global wavefields for local 3D structures by wavefield injection and extrapolation. *Geophysical Journal International*, 225, 1782, 1798. <https://doi.org/10.1093/gji/ggaa563>
- Plessix, R.-E. (2006). A review of the adjoint-state method for computing the gradient of a functional with geophysical applications. *Geophysical Journal International*, 167(2), 495–503. <https://doi.org/10.1111/j.1365-246x.2006.02978.x>
- Pratt, R. G. (1999). Seismic waveform inversion in the frequency domain: Part 1: Theory and verification in a physical scale model. *Geophysics*, 64(3), 888–901. <https://doi.org/10.1190/1.1444597>
- Raikes, S. A. (1980). Regional variations in upper mantle structure beneath southern California. *Geophysical Journal International*, 63(1), 187–216. <https://doi.org/10.1111/j.1365-246x.1980.tb02616.x>
- Ritzwoller, M. H., Shapiro, N. M., Barmin, M. P., & Levshin, A. L. (2002). Global surface wave diffraction tomography. *Journal of Geophysical Research*, 107(B12). <https://doi.org/10.1029/2002jb001777>
- Sager, K., Boehm, C., Ermert, L., Krischer, L., & Fichtner, A. (2020). Global-scale full-waveform ambient noise inversion. *Journal of Geophysical Research: Solid Earth*, 125(4), e2019JB018644. <https://doi.org/10.1029/2019jb018644>
- Sager, K., Ermert, L., Boehm, C., & Fichtner, A. (2018). Toward full waveform ambient noise inversion. *Geophysical Journal International*, 212(1), 566–590. <https://doi.org/10.1093/gji/ggx429>
- Saygin, E., & Kennett, B. L. (2010). Ambient seismic noise tomography of Australian continent. *Tectonophysics*, 481(1–4), 116–125. <https://doi.org/10.1016/j.tecto.2008.11.013>
- Schmandt, B., & Humphreys, E. (2010). Complex subduction and small-scale convection revealed by body-wave tomography of the western United States upper mantle. *Earth and Planetary Science Letters*, 297(3–4), 435–445. <https://doi.org/10.1016/j.epsl.2010.06.047>
- Shapiro, N. M., Campillo, M., Stehly, L., & Ritzwoller, M. H. (2005). High-resolution surface-wave tomography from ambient seismic noise. *Science*, 307(5715), 1615–1618. <https://doi.org/10.1126/science.1108339>
- Shen, W., Ritzwoller, M. H., & Schulte-Pelkum, V. (2013). A 3-D model of the crust and uppermost mantle beneath the Central and Western US by joint inversion of receiver functions and surface wave dispersion. *Journal of Geophysical Research: Solid Earth*, 118(1), 262–276. <https://doi.org/10.1029/2012jb009602>
- Sigloch, K., McQuarrie, N., & Nolet, G. (2008). Two-stage subduction history under North America inferred from multiple-frequency tomography. *Nature Geoscience*, 1(7), 458, 462. <https://doi.org/10.1038/ngeo231>
- Sun, M., Zhang, J., & Zhang, W. (2017). Alternating first-arrival traveltimes tomography and waveform inversion for near-surface imaging. *Geophysics*, 82(4), R245–R257. <https://doi.org/10.1190/geo2016-0576.1>
- Tao, K., Grand, S. P., & Niu, F. (2018). Seismic structure of the upper mantle beneath eastern Asia from full waveform seismic tomography. *Geochemistry, Geophysics, Geosystems*, 19(8), 2732–2763. <https://doi.org/10.1029/2018gc007460>
- Tape, C., Liu, Q., Maggi, A., & Tromp, J. (2009). Adjoint tomography of the southern California crust. *Science*, 325(5943), 988–992. <https://doi.org/10.1126/science.1175298>
- Tape, C. H. (2009). *Seismic tomography of southern California using adjoint methods (Unpublished doctoral dissertation)*. California Institute of Technology.
- Tong, P., Chen, C.-w., Komatitsch, D., Basini, P., & Liu, Q. (2014). High-resolution seismic array imaging based on an SEM-FK hybrid method. *Geophysical Journal International*, 197(1), 369–395. <https://doi.org/10.1093/gji/ggt508>
- Tong, P., Komatitsch, D., Tseng, T.-L., Hung, S.-H., Chen, C.-W., Basini, P., & Liu, Q. (2014). A 3-D spectral-element and frequency-wave number hybrid method for high-resolution seismic array imaging. *Geophysical Research Letters*, 41(20), 7025–7034. <https://doi.org/10.1002/2014gl061644>
- Tromp, J. (2020). Seismic wavefield imaging of Earth's interior across scales. *Nature Reviews Earth & Environment*, 1, 40–53. <https://doi.org/10.1038/s43017-019-0003-8>
- Tromp, J., Luo, Y., Hanasoge, S., & Peter, D. (2010). Noise cross-correlation sensitivity kernels. *Geophysical Journal International*, 183(2), 791–819. <https://doi.org/10.1111/j.1365-246x.2010.04721.x>
- Tromp, J., Tape, C., & Liu, Q. (2005). Seismic tomography, adjoint methods, time reversal and banana-donut kernels. *Geophysical Journal International*, 160(1), 195–216.
- Tsai, V. C. (2009). On establishing the accuracy of noise tomography travel-time measurements in a realistic medium. *Geophysical Journal International*, 178(3), 1555–1564. <https://doi.org/10.1111/j.1365-246x.2009.04239.x>
- van der Hilst, R. D., Widiyantoro, S., & Engdahl, E. (1997). Evidence for deep mantle circulation from global tomography. *Nature*, 386(6625), 578–584. <https://doi.org/10.1038/386578a0>
- Virieux, J., & Operto, S. (2009). An overview of full-waveform inversion in exploration geophysics. *Geophysics*, 74(6), WCC1–WCC26. <https://doi.org/10.1190/1.3238367>
- Wang, K., Jiang, C., Yang, Y., Schulte-Pelkum, V., & Liu, Q. (2020). Crustal deformation in southern California constrained by radial anisotropy from ambient noise adjoint tomography. *Geophysical Research Letters*, 47(12), e2020GL088580. <https://doi.org/10.1029/2020gl088580>
- Wang, K., Liu, Q., & Yang, Y. (2019). Three-dimensional sensitivity kernels for multicomponent empirical Green's functions from ambient noise: Methodology and application to adjoint tomography. *Journal of Geophysical Research: Solid Earth*, 124(6), 5794–5810. <https://doi.org/10.1029/2018jb017020>
- Wang, K., Luo, Y., & Yang, Y. (2016). Correction of phase velocity bias caused by strong directional noise sources in high-frequency ambient noise tomography: A case study in Karamay, China. *Geophysical Journal International*, 205(2), 715–727. <https://doi.org/10.1093/gji/ggw039>
- Wang, K., Yang, Y., Basini, P., Tong, P., Tape, C., & Liu, Q. (2018). Refined crustal and uppermost mantle structure of southern California by ambient noise adjoint tomography. *Geophysical Journal International*, 215(2), 844–863. <https://doi.org/10.1093/gji/ggy312>

- Wang, Y., Chevrot, S., Monteiller, V., Komatitsch, D., Mouthereau, F., Manatschal, G., et al. (2016). The deep roots of the western Pyrenees revealed by full waveform inversion of teleseismic P waves. *Geology*, *44*(6), 475–478. <https://doi.org/10.1130/g37812.1>
- Wang, Y., Forsyth, D. W., Rau, C. J., Carriero, N., Schmandt, B., Gaherty, J. B., & Savage, B. (2013). Fossil slabs attached to unsubsided fragments of the Farallon plate. *Proceedings of the National Academy of Sciences*, *110*(14), 5342–5346. <https://doi.org/10.1073/pnas.1214880110>
- West, M., Gao, W., & Grand, S. (2004). A simple approach to the joint inversion of seismic body and surface waves applied to the southwest US. *Geophysical Research Letters*, *31*(15). <https://doi.org/10.1029/2004gl020373>
- Woodhouse, J. H., & Dziewonski, A. M. (1984). Mapping the upper mantle: Three-dimensional modeling of Earth structure by inversion of seismic waveforms. *Journal of Geophysical Research*, *89*(B7), 5953–5986. <https://doi.org/10.1029/jb089ib07p05953>
- Xie, J., Chu, R., & Yang, Y. (2018). 3-D upper-mantle shear velocity model beneath the contiguous United States based on broadband surface wave from ambient seismic noise. *Pure and Applied Geophysics*, *175*(10), 3403–3418. <https://doi.org/10.1007/s00024-018-1881-2>
- Yang, X., & Gao, H. (2020). Segmentation of the Aleutian-Alaska subduction zone revealed by full-wave ambient noise tomography: Implications for the along-strike variation of volcanism. *Journal of Geophysical Research: Solid Earth*, *125*(11), e2020JB019677. <https://doi.org/10.1029/2020jb019677>
- Yang, Y., Ritzwoller, M. H., Levshin, A. L., & Shapiro, N. M. (2007). Ambient noise Rayleigh wave tomography across Europe. *Geophysical Journal International*, *168*(1), 259–274. <https://doi.org/10.1111/j.1365-246x.2006.03203.x>
- Yang, Y., Ritzwoller, M. H., Lin, F.-C., Moschetti, M., & Shapiro, N. M. (2008). Structure of the crust and uppermost mantle beneath the western United States revealed by ambient noise and earthquake tomography. *Journal of Geophysical Research: Solid Earth*, *113*(B12). <https://doi.org/10.1029/2008jb005833>
- Yao, H., & Van Der Hilst, R. D. (2009). Analysis of ambient noise energy distribution and phase velocity bias in ambient noise tomography, with application to SE Tibet. *Geophysical Journal International*, *179*(2), 1113–1132. <https://doi.org/10.1111/j.1365-246x.2009.04329.x>
- Yao, H., van Der Hilst, R. D., & De Hoop, M. V. (2006). Surface-wave array tomography in SE Tibet from ambient seismic noise and two-station analysis—I. Phase velocity maps. *Geophysical Journal International*, *166*(2), 732–744. <https://doi.org/10.1111/j.1365-246x.2006.03028.x>
- Zandt, G., Gilbert, H., Owens, T. J., Ducea, M., Saleeby, J., & Jones, C. H. (2004). Active foundering of a continental arc root beneath the southern Sierra Nevada in California. *Nature*, *431*(7004), 41–46. <https://doi.org/10.1038/nature02847>
- Zhang, C., Yao, H., Liu, Q., Zhang, P., Yuan, Y. O., Feng, J., & Fang, L. (2018). Linear array ambient noise adjoint tomography reveals intense crust-mantle interactions in North China Craton. *Journal of Geophysical Research: Solid Earth*, *123*(1), 368–383. <https://doi.org/10.1002/2017jb015019>
- Zhang, C., Yao, H., Tong, P., Liu, Q., & Lei, T. (2020). Joint inversion of linear array ambient noise surface-wave and teleseismic body-wave data based on an adjoint-state method. *Acta Geophysica Sinica*, *63*(11), 4065–4079.
- Zhang, H., Maceira, M., Roux, P., & Thurber, C. (2014). Joint inversion of body-wave arrival times and surface-wave dispersion for three-dimensional seismic structure around SAFOD. *Pure and Applied Geophysics*, *171*(11), 3013–3022. <https://doi.org/10.1007/s00024-014-0806-y>
- Zheng, S., Sun, X., Song, X., Yang, Y., & Ritzwoller, M. H. (2008). Surface wave tomography of China from ambient seismic noise correlation. *Geochemistry, Geophysics, Geosystems*, *9*(5). <https://doi.org/10.1029/2008gc001981>
- Zhou, Y., Dahlen, F., & Nolet, G. (2004). Three-dimensional sensitivity kernels for surface wave observables. *Geophysical Journal International*, *158*(1), 142–168. <https://doi.org/10.1111/j.1365-246x.2004.02324.x>
- Zhu, H., Bozdağ, E., Peter, D., & Tromp, J. (2012). Structure of the European upper mantle revealed by adjoint tomography. *Nature Geoscience*, *5*(7), 493–498. <https://doi.org/10.1038/ngeo1501>